Oxygen Mass Transfer Calculations in Large Arteries

J. A. Moore

C. R. Ethier

Department of Mechanical Engineering and
Institute of Biomedical Engineering,
University of Toronto,
Toronto, Ontario, Canada

The purpose of this study was to model the transport of oxygen in large arteries, including the physiologically important effects of oxygen transport by hemoglobin, coupling of transport between oxygen in the blood and in wall tissue, and metabolic consumption of oxygen by the wall. Numerical calculations were carried out in an 89 percent area reduction axisymmetric stenosis model for several wall thicknesses. The effects of different boundary conditions, different schemes for linearizing the oxyhemoglobin saturation curve, and different Schmidt numbers were all examined by comparing results against a reference solution obtained from solving the full nonlinear governing equations with physiologic values of Schmidt number. Our results showed that for parameters typical of oxygen mass transfer in the large arteries, oxygen transport was primarily determined by wall-side effects, specifically oxygen consumption by wall tissue and wall-side mass transfer resistance. Hemodynamic factors played a secondary role, producing maximum local variations in intimal oxygen tension on the order of only 5–6 mmHg. For purposes of modeling blood-side oxygen transport only, accurate results were obtained through use of a computationally efficient linearized form of the convection-diffusion equation, so long as blood-side oxygen tensions remained in the physiologic range for large arteries. Neglect of oxygen binding by hemoglobin led to large errors, while arbitrary reduction of the Schmidt number led to more modest errors. We conclude that further studies of oxygen transport in large arteries must couple blood-side oxygen mass transport to transport in the wall, and accurately model local oxygen consumption within the wall.

1 Introduction

Arterial transport of blood-borne materials is essential for maintenance of normal arterial wall physiology. Disturbed transport of such materials, due for example to altered hemodynamic patterns caused by local geometric factors, may be linked to the pathogenesis of vascular diseases. One such blood-borne species, which is of major interest, is oxygen, since it is an important cellular metabolite. Abnormalities in arterial wall oxygen tension have been implicated in the formation of atherosclerotic lesions [1–4], and may also be linked to intimal hyperplasia [5].

Analysis of oxygen transport in arteries is complicated by two factors. First, oxygen transport in blood is coupled to oxygen transport and consumption in the artery wall. Second, oxygen in blood is carried in two forms: as free oxygen dissolved in plasma, and bound to hemoglobin (Hb) within red cells. Due to the nonlinear dependence of oxyhemoglobin concentration on plasma oxygen partial pressure (PO_2), blood-side oxygen transport is a strongly nonlinear mass transfer problem. These complications prevent use of simple *in vitro* experimental models, necessitating either *in vivo* experimental measurements of oxygen tension [5, 6], or numerical modeling of oxygen transport (e.g., [7–11]).

The goal of the present paper is to study oxygen transport in blood and the arterial wall via a numerical modeling approach. We incorporate a number of physiologically important factors, including oxygen consumption by cells in the artery wall, coupling of oxygen transport between blood and the wall, and the nonlinear oxygen binding properties of hemoglobin. Additionally, we study different ways of treating the nonlinearity in blood-side oxygen mass transfer, and the Schmidt number dependence of the results. The analysis is carried out in a physiologically relevant axisymmetric stenosis geometry under steady flow conditions.

2 Methods

2.1 Governing Equations. Considering oxygen dissolved in plasma and that bound to hemoglobin as two distinct species, the following coupled convection-diffusion equations describe oxygen transport in blood:

$$\alpha \frac{\partial PO_2}{\partial t} = \alpha \nabla \cdot (D_b \nabla PO_2) + r \tag{1}$$

$$[\mathrm{Hb}] \frac{\partial S}{\partial t} = [\mathrm{Hb}] \nabla \cdot (D_c \nabla S) - r \tag{2}$$

where r is the rate of O_2 release by the carrier Hb, $\partial/\partial t$ is the substantive derivative, computed using the blood velocity field, α is the solubility of oxygen in plasma, S is the oxyhemoglobin saturation function (see below), PO_2 is the plasma oxygen tension, [Hb] is the total oxygen carrying capacity of hemoglobin in blood, and D_b and D_c are the diffusivities of free oxygen in blood and of oxyhemoglobin in blood, respectively. Note that we have treated [Hb] as a constant in Eq. (2), which implies a spatially uniform distribution of hemoglobin in the region of interest. Consistent with this approximation, we ignore the presence of the plasma skimming layer, which is much thinner than even the mass transfer boundary layers, and which has been shown to have a very small effect on overall oxygen transport [8]. Because the oxyhemoglobin is contained inside red cells, D_c is usually interpreted as the diffusion coefficient of a red cell, which is effectively zero. However, it is known that red cells in shear flow undergo significant dispersion [12], and therefore in the present work we interpret D_c to be the shear-augmented dispersion coefficient of a red cell.

Contributed by the Bioengineering Division for publication in the JOURNAL OF BIOMECHANICAL ENGINEERING. Manuscript received by the Bioengineering Division May 23, 1996; revised manuscript received November 14, 1996. Associate Technical Editor: D. N. Ku.

Addition of Eqs. (1) and (2) yields a single convection-diffusion equation for PO_2:

$$\left(1 + \frac{[\mathrm{Hb}]}{\alpha}\frac{dS}{dPO_2}\right)\frac{\mathcal{D}PO_2}{\mathcal{D}t} = \nabla\cdot\left[D_b\left(1 + \frac{[\mathrm{Hb}]}{\alpha}\frac{D_c}{D_b}\frac{dS}{dPO_2}\right)\nabla PO_2\right] \quad (3)$$

The saturation function, S, defined as the ratio of oxyhemoglobin to total hemoglobin, is approximated by the Hill equation:

$$S = \frac{PO_2^n}{PO_2^n + P_{50}^n} \quad (4)$$

where $n = 2.7$ and $P_{50} = 26.6$ mmHg.

The coefficient $1 + ([\mathrm{Hb}]/\alpha)(dS/dPO_2)$ on the left-hand side of Eq. (3) can be interpreted as a nonconstant oxygen carrying capacity, while $D_b[1 + ([\mathrm{Hb}]/\alpha)(D_c/D_b)(dS/dPO_2)]$ is a nonconstant diffusivity. Since each of these coefficients depends on plasma oxygen tension through the term dS/dPO_2, it is seen that there are two mechanisms whereby nonlinearity enters the governing equations.

2.1.1 Linearization of the Blood-Side Equation. Due to its nonlinear nature, solution of Eq. (3) is computationally intensive. It is therefore advantageous to linearize Eq. (3) by replacing dS/dPO_2 by some suitable constant mean value, $\overline{dS/dPO_2}$ [7, 13, 14], here obtained by first-order Taylor series expansion of S as given by the Hill equation. This yields

$$\frac{\overline{dS}}{dPO_2} = \frac{n\bar{S}}{\overline{PO_2}}(1 - \bar{S}) \quad (5)$$

where $\overline{PO_2}$ is some reference value of PO_2, and $\bar{S}$ is S evaluated at $\overline{PO_2}$. The value of $\overline{PO_2}$ should be selected so as to minimize the error in the approximation to dS/dPO_2 over the working range of oxygen tensions, and is therefore boundary condition dependent. Unless otherwise noted, we used a $\overline{PO_2}$ value of 75 mmHg.

Colton et al. [14] showed that linearization schemes could be a poor approximation for analyzing blood flow in the microcirculation; however, the accuracy of this simplification for oxygen mass transfer in the large arteries, where local variations in oxygen tension are less than in the microcirculation, has not been quantified.

Equation (5) can be used to linearize the left-hand side, the right-hand side, or both sides of equation (3). Additional simplifications result from setting D_c to zero, as is often done, or by ignoring the presence of oxyhemoglobin completely. In the first phase of this study, we tested the effects of these simplifications by computing blood-side oxygen transport for the following five cases:

1 *Reference solution:* all terms and all nonlinearity in Eq. (3) are retained.

2 *Fully linearized solution:* all terms in Eq. (3) are retained, and both sides of the equation are linearized using Eq. (5).

3 *Nonlinear solution with no oxyhemoglobin dispersion:* D_c is set to zero, but nonlinearity is retained on the left side of Eq. (3).

4 *Linearized solution with no oxyhemoglobin dispersion:* D_c is set to zero, and the left side of Eq. (3) is linearized using Eq. (5).

5 *No hemoglobin:* [Hb] is set to zero.

2.1.2 Schmidt Number Effects. As is the case for all but the smallest of blood-borne species, the Schmidt number for oxygen in blood is very large. This implies that the mass transfer boundary layer will be very thin, which in turn necessitates use of extremely high computational grid densities near the artery wall. In practice, this is difficult to achieve, with the result that grid (or cell) Peclet numbers can be large. Many numerical schemes demonstrate poor convergence and accuracy for large cell Peclet numbers. To overcome these difficulties, stabilized numerical schemes can be used [10], or the Schmidt number can be reduced, e.g., [15].

The error associated with reducing the Schmidt number does not appear to have been quantified for flow situations typical of the large arteries. In the second phase of the study, we investigated the Schmidt number dependence of blood-side oxygen mass transfer by arbitrarily reducing Sc from its physiological value by a factor of either 100 or 1000.

2.1.3 Blood-Wall Transport Coupling. In the third phase of the study, blood-side oxygen mass transport was coupled to oxygen transport and consumption in the artery wall. A typical filtrate (convective) velocity within the artery wall is 10^{-6} cm/s [16], while oxygen diffusion velocity scales as D_T/t, where D_T is the oxygen diffusivity in tissue and t is the wall thickness (inner lumen to vasa vasorum). Using $D_T \approx 0.9 \times 10^{-9}$ m^2/s, t values from 4–12.5 percent of the arterial diameter (see Section 2.2), and a typical arterial diameter of 1 cm, gives diffusion velocities of order 10^{-5} to 10^{-4} cm/s. Convective transport of oxygen within the artery wall was therefore neglected, since filtrate velocities are one to two orders of magnitude smaller than oxygen diffusion velocities (see also [16]). Thus, the equation governing wall-side oxygen transport was:

$$\alpha_T\frac{dPO_2}{dt} = \alpha_T\nabla\cdot(D_T\nabla PO_2) + \dot{q} \quad (6)$$

where $\dot{q}$ represents a constant volumetric consumption rate of oxygen by cells within the arterial wall tissue. Continuity of both PO_2 and oxygen flux were required across the blood–tissue interface.

2.2 Computational Geometry and Model. All mass transfer calculations were carried out in a rigid-walled axisymmetric cosine-shaped stenosis model, with maximum lumenal area reduction 88.9 percent (Fig. 1(*a*)). The stenosis extended two artery diameters on either side of the throat. For simulations that included the effects of oxygen transport within the arterial wall, the computational domain consisted of the arterial lumen

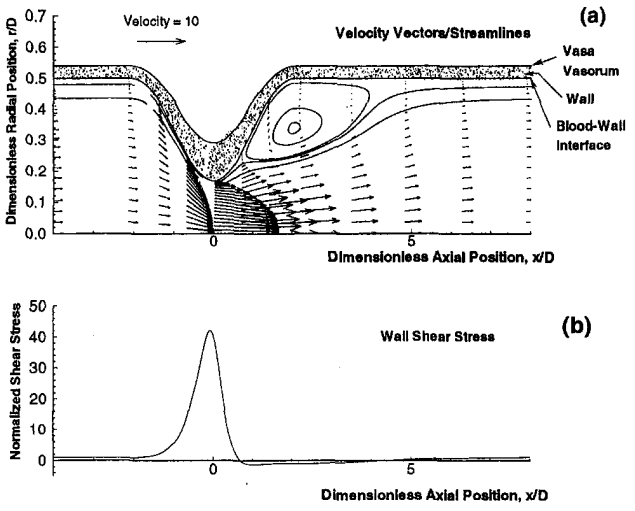

Fig. 1 Model geometry and velocity vector plot [panel (*a*)] and resulting normalized wall shear stress distribution [panel (*b*)] for steady flow through the stenosis. In panel (*a*), the velocity vectors are normalized by the spatial mean inlet velocity, and the solid lines are streamlines. In panel (*b*) the shear stress is normalized by the Poiseuille wall shear stress in an artery without a stenosis at the same Reynolds number. Note the unequal axis scaling in panel (*a*).

plus the region of the artery wall from the inner surface of the intima to the vasa vasorum, i.e., the outer boundary of the computational domain was taken as the location of the vasa vasorum. Specifically, far from the stenosis, the distance from the intima to the vasa vasorum was 4 percent of the unstenosed lumenal diameter, consistent with a healthy human abdominal aorta [17], while in the region of the stenosis this distance increased to a maximum value (at the throat) equal to 12.5 percent of the unstenosed lumenal diameter. This gave a geometry in which the diameter of the vasa vasorum decreased close to the stenosis, consistent with data showing peristenotic proliferation of the vasa vasorum [2]. A "thin-walled" stenosis model was also created, which differed from the model described above in that the artery wall reached a maximum thickness of only 9.5 percent of the unstenosed lumenal diameter. This model has the advantages of being clinically relevant, of demonstrating moderately complex flow patterns (i.e., the recirculation zone distal to the stenosis throat), and of having been used previously for simplified blood-side oxygen mass transfer calculations [9]. It is also a fairly simple geometry, which, because of its two-dimensional nature, is amenable to parametric numerical studies.

For the blood velocity field calculation, used in all subsequent mass transfer computations, steady flow of a Newtonian fluid with an inlet Reynolds number Re_D of 50 was modeled. Fully developed flow was specified at the inlet, the no-slip condition was specified at the vessel wall, and zero traction was specified at the outlet. Blood density and viscosity were taken to be 1000 kg/m^3 and 3.5×10^{-3} kg/m·s, respectively. For mass transfer calculations, the inlet condition was a uniform oxygen tension of 85 mmHg, while zero axial gradient in oxygen partial pressure was imposed at the outlet. For phases one and two of the study, which examined only blood-side mass transfer, no calculations were carried out in the wall, and the following boundary conditions were used at the blood–wall interface:

1 A constant wall oxygen tension of 0 mmHg. Although this is not physiologic, it was included because it is the most severe test of linearizing the blood-side transport equation, demonstrating the maximum possible variation in the slope of the oxyhemoglobin saturation function. For this boundary condition, PO_2 was taken as 50 mmHg.
2 A constant wall oxygen tension of 60 mmHg. This boundary condition is considered to be more physiologic, since the oxygen wall tension measured in dogs *in vivo* is approximately 60 mmHg [6].

For the third phase of the study, examining blood–wall coupling, a constant oxygen tension of 45 mmHg was maintained at the outer boundary of the computational domain, i.e., at the assumed location of the vasa vasorum.

All flow field and mass transfer calculations were performed using the commercial code Fluent (Creare.x, Hanover, NH). The computational domain extended four diameters upstream of the stenosis throat and 16 diameters downstream. Based on preliminary grid convergence studies, most calculations were performed on a grid with 500 nodes in the axial direction and 103 nodes in the radial direction. Nonuniform spacing was used, such that the off-wall spacing of the first grid point at the stenosis throat was 4.7×10^{-4} artery diameters. The power law scheme was used for spatial differencing. Parameter values for all simulations were as follows: [Hb] = 0.2 ml O_2/ml blood [7]; $D_b = 1.2 \times 10^{-9}$ m^2/s [18]; $D_c = 1.5 \times 10^{-11}$ m^2/s [12]; $\alpha = 2.5 \times 10^{-5}$ ml O_2/ml blood/mmHg [8]; $D_T = 0.9 \times 10^{-9}$ m^2/s [8]; $\alpha_T = 2.4 \times 10^{-5}$ ml O_2/ml tissue/mmHg [8]; and $\dot{q} = 2.1 \times 10^{-5}$ ml O_2/ml tissue/s [8].

Oxygen wall fluxes are presented in terms of the local Sherwood number, Sh_D, defined as

$$Sh_D = \frac{q_w D}{D_b(PO_{2in} - PO_{2ref})} \tag{7}$$

where q_w is the local wall oxygen flux, D is the arterial diameter, PO_{2in} and PO_{2ref} are the specified inlet and reference oxygen tensions, respectively. For calculations involving blood-side mass transfer only, PO_{2ref} was the specified wall tension. For coupled blood–wall calculations, PO_{2ref} was the specified vasa vasorum tension. In evaluating q_w, account was taken of the variation of the oxygen tension with PO_2, i.e., q_w was computed as:

$$q_w = -D_b\left(1 + \frac{[\mathrm{Hb}]}{\alpha}\frac{D_c}{D_b}\frac{dS}{dPO_2}\right)\frac{\partial PO_2}{\partial n} \tag{8}$$

where n is the normal to the wall, with appropriate modification for the cases where $D_c = 0$, [Hb] = 0, or the oxyhemoglobin saturation curve was linearized.

3 Results

3.1 Flow Field. It is useful to point out the main features of the flow field (Fig. 1(*a*)), which include a prominent jet through and distal to the stenosis throat, and separation adjacent to the wall distal to the throat. As can be seen from the corresponding plot of normalized wall shear stress (Fig. 1(*b*)), this leads to very large wall shear stresses at the throat, and zero values at the separation and reattachment points, located at $x/D = 0.70$ and 4.25, respectively. Computed velocity fields were validated against published results [9] as well as the solution obtained from our well-validated in-house Navier–Stokes solver [19].

3.2 Blood Side Effects: Effects of Linearization. We first examine the mass transfer solution for the simplest case, i.e., that of no hemoglobin (Case 5), since it allows a simple physical interpretation and can be compared to the analogous calculations of Schneiderman et al. [9]. Figure 2(*a*) shows

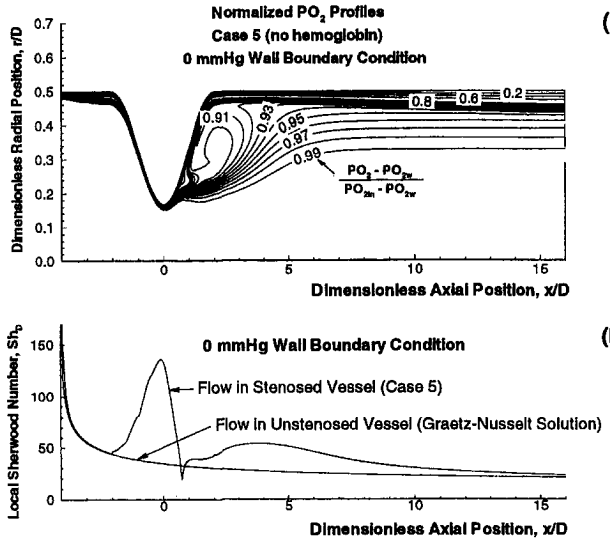

Fig. 2 Normalized isoconcentration contours [panel (*a*)] and local Sherwood number as a function of axial position [panel (*b*)] for Case 5 (no hemoglobin present) with 0 mmHg oxygen wall tension boundary condition. The contoured variable in panel (*a*) is the dimensionless oxygen partial pressure, $(PO_2 - PO_{2w})/(PO_{2in} - PO_{2w})$, where PO_{2w} and PO_{2in} are the wall and inlet oxygen plasma partial pressures, respectively. Note that the contours in panel (*a*) are not uniformly spaced. In panel (*b*), the Lévêque solution of the Graetz–Nusselt problem [22] is also plotted for reference. Small slope discontinuities seen in the numerical solution are due to small changes in the wall slope in the computational domain, and are not indicative of mesh underresolution.

normalized isoconcentration contours for this case with the 0 mmHg oxygen wall tension boundary condition. Proximal to the stenosis, normal growth of the mass transfer boundary layer with axial position is evident. The recirculation zone distal to the stenosis throat has two major effects. First, at the separation point, recirculating blood from the near wall region having very low oxygen tension is convected away from the wall, forming a small pocket of oxygen-depleted blood. Second, relatively oxygen-rich blood is convected toward the wall in the vicinity of the reattachment point, forming a zone of higher oxygen tension on either side of the reattachment point. These features are similar to those observed by Schneiderman et al. in their study [9], although quantitative comparison was not carried out due to the fact that they used an approximate form of the velocity field to compute their concentration field.

Corresponding to the above isoconcentration plot, Fig. 2(*b*) shows the local Sherwood number as a function of axial position for Case 5 with the 0 mmHg oxygen wall tension boundary condition. Also shown is the analytical Graetz–Nusselt solution for the developing mass transfer boundary layer in a straight tube. Relatively large Sherwood numbers are observed at the throat of the stenosis, consistent with high shear rates there. In the neighborhood of the separation point, a Sherwood number below that predicted by the Graetz–Nusselt solution is seen, which can be attributed to the "pocket" of low-oxygen-tension blood described above. Finally, on either side of the reattachment point, the Sherwood number exceeds that of the Graetz–Nusselt solution, due to the convection of oxygen-rich blood toward the wall, as described above.

Figure 3 shows a comparison of the local Sherwood number for all five cases identified above, for the 0 mmHg oxygen wall tension boundary condition. All curves show qualitatively similar behaviour, consistent with the description in the above paragraph. However, there are major differences in the magnitudes of the Sherwood numbers, particularly near the throat of the stenosis. Interestingly, the dynamic range (peak Sherwood number divided by minimum Sherwood number) was quite similar for all cases (Table 1). It is seen that the solution that comes closest to the reference case (Case 1) is that obtained by linearizing the governing equation and retaining red cell dispersion effects (Case 2). Solutions in which the dispersion of red cells was neglected (Cases 3 and 4) are further from the reference case, while the solution that neglects hemoglobin (Case 5) shows major differences from the reference case.

Figure 4 compares normalized isoconcentration contours for the reference solution (Case 1) and the fully linearized solution (Case 2), both for the 0 mmHg oxygen wall tension boundary

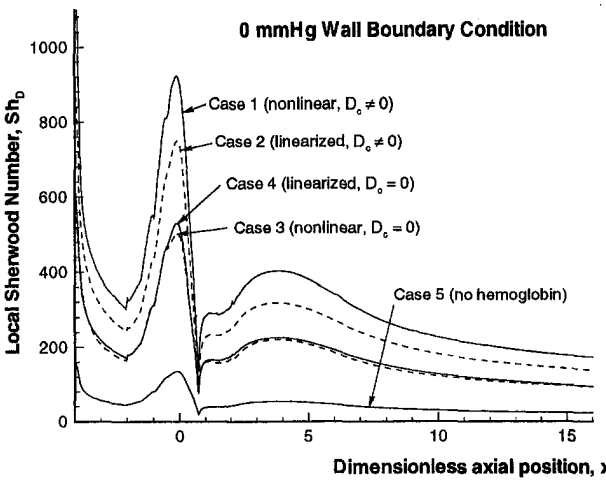

Fig. 3 Local Sherwood number, Sh_D, as a function of dimensionless axial position for all five cases with 0 mmHg oxygen wall tension boundary condition. Refer to text for full description of cases.

Table 1 Maximum Sherwood number, minimum Sherwood number, and ratio of maximum to minimum observed for each of Cases 1–5. 0 mmHg and 60 mmHg refer to cases run with 0 mmHg and 60 mmHg wall oxygen tension boundary conditions, respectively.

	0 mmHg			60 mmHg		
Case	Max Sh_D	Min Sh_D	Ratio	Max Sh_D	Min Sh_D	Ratio
1	920.6	134.4	6.85	389.7	49.5	7.87
2	747.4	102.9	7.26	389.8	49.8	7.83
3	500.3	91.5	5.47	332.4	42.9	7.75
4	530.0	75.7	7.00	346.3	44.9	7.71
5	135.3	19.9	6.80	135.3	19.9	6.80

condition. Surprisingly, even though these two cases showed somewhat similar local Sherwood number profiles, their isoconcentration contours exhibit major differences.

Figure 5 shows local Sherwood number as a function of position for all five cases for the more physiologic 60 mmHg oxygen wall tension boundary condition. Although there are differences between all five cases, the magnitude of these differences is much less than that observed for the 0 mmHg wall tension boundary condition. In fact, Cases 1 and 2 yield essentially identical local Sherwood number distributions, with Cases 3 and 4 showing a modest reduction in peak values. However, Case 5 (no hemoglobin) once again shows major differences with respect to the reference case.

3.3 Blood-Side Transport: Effects of Changing Sc. In Fig. 6 we plot the scaled local Sherwood number as a function of position for Case 2 with 60 mmHg oxygen wall tension. Data are shown for three different values of the Schmidt number: the physiologic value of $\nu/D_b = 2917$, and reduced values of 29.17 and 2.917, obtained by increasing both D_b and D_c by 100 or 1000, respectively.[1] Although Sherwood number profiles scaled by $Sc^{1/3}$ are qualitatively similar as the Schmidt number is reduced, there are important quantitative differences. Specifically, reducing Sc tends to reduce the magnitudes of the extrema in the scaled Sherwood number plots. Furthermore, some of

[1] Although the nominal value of Schmidt number, based on ν and D_b, is 2917, the effective value is much larger. Equation (3) shows that the term $D_b[1 + ([\mathrm{Hb}]/\alpha)(D_c/D_b)(dS/dPO_2)]/[1 + ([\mathrm{Hb}]/\alpha)(dS/dPO_2)]$ can be interpreted as a local effective oxygen diffusivity. For the conditions of Case 2, this term equals $0.0721\,D_b$, and the value of the Schmidt number formed with this effective diffusivity is 40,521.

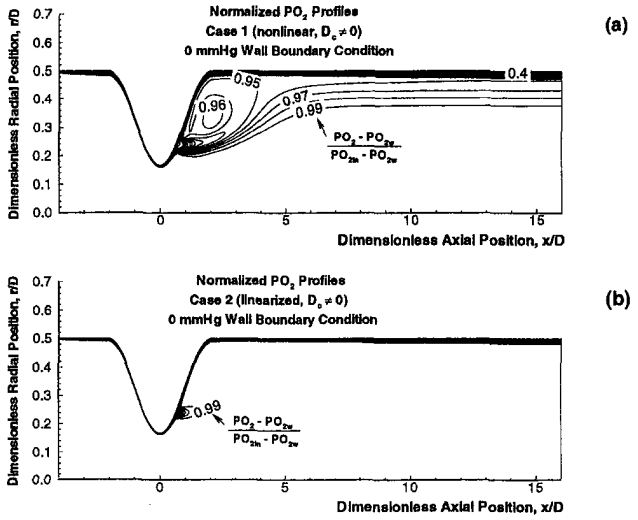

Fig. 4 Normalized isoconcentration contours for Case 1 (reference solution; panel (*a*)) and Case 2 (linearized solution with $D_c \neq 0$; panel (*b*)) for 0 mmHg oxygen wall tension boundary condition. The contoured variable is as defined in Fig. 2. Note that the contours are not uniformly spaced.

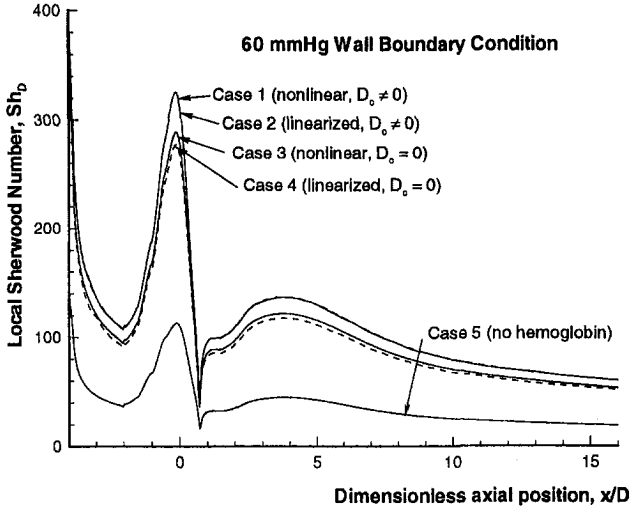

Fig. 5 Local Sherwood number, Sh_D, as a function of dimensionless axial position for all 5 cases for 60 mmHg oxygen wall tension boundary condition. Lines for Cases 1 and 2 are essentially coincident. Refer to text for full description of cases, and compare with Fig. 3.

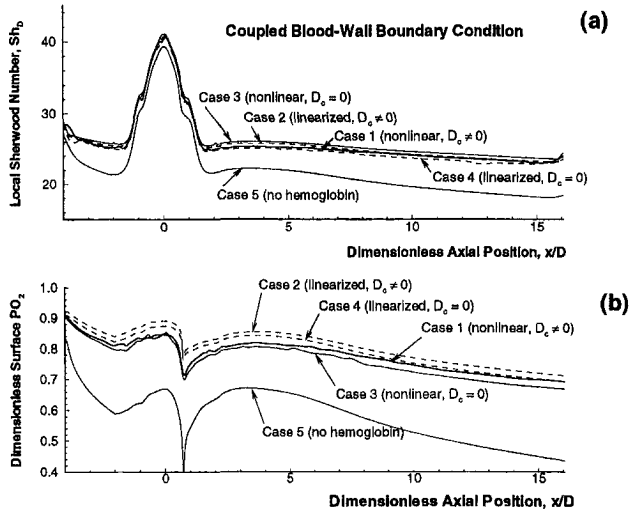

Fig. 7 Local Sherwood number, Sh_D [panel (*a*)] and dimensionless surface PO_2 [panel (*b*)] as a function of dimensionless axial position for all five cases with fluid side transport coupled to an oxygen consuming wall. Refer to text for full description of cases. Model geometry is as shown in Fig. 1(*b*).

the local detail in the recirculation region (dimensionless axial position of 0.8 to 2.0) is absent in the runs with reduced Schmidt number. The lower Schmidt number also thickens the mass transfer boundary layer, and therefore produces substantially different concentration fields as compared to the physiologic case (data not shown).

3.4 Blood-Wall Transport Coupling. Figure 7(*a*) shows the local Sherwood number as a function of position for all five cases under the condition of coupled blood–wall oxygen transport. As was the situation for the 60 mmHg constant wall tension boundary condition, differences between cases are relatively minor, with the exception of Case 5 (no hemoglobin), which once again shows major differences with respect to the reference case.

Comparison of Figs. 7(*a*) and 5 shows three important aspects of simulations done with coupled blood–wall transport:

- Oxygen flux is quite symmetric about the stenosis throat and its local magnitude is approximately proportional to wall thickness when blood–wall transport coupling is present.
- Hemodynamically driven features seen with constant wall tension boundary conditions, such as the dip in local Sherwood number at the separation point, are largely absent when blood–wall transport coupling is present.
- Peak Sherwood number magnitudes are approximately tenfold lower when blood–wall transport coupling is present.

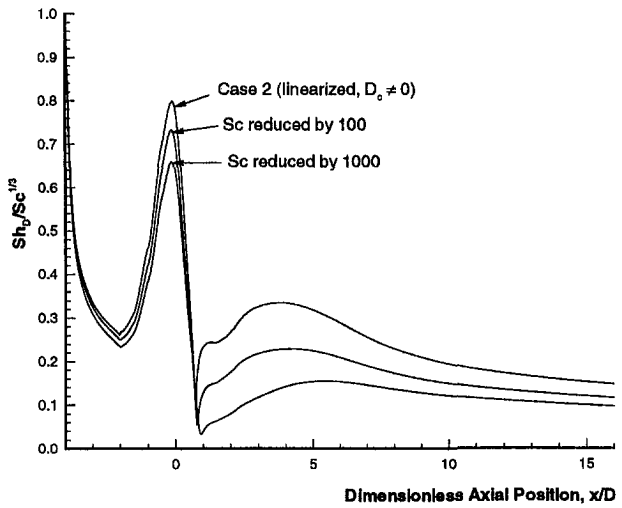

Fig. 6 Scaled local Sherwood number as a function of axial position for Case 2 with 60 mmHg oxygen wall tension, and three different values of Schmidt number. Refer to text for full description of Case 2. Following the scaling in the Graetz–Nusselt solution, the vertical axis is the Sherwood number normalized by the cube root of the Schmidt number.

The first observation suggests that local oxygen flux is determined by local wall-side oxygen demand, which is proportional to local wall thickness. This is supported by the data shown in Fig. 8(*a*), demonstrating a significant reduction in local Sherwood number when wall thickness is reduced. Since the hemodynamics in the "thin-walled" and regular models are identical, this indicates that oxygen flux into the artery wall is primarily determined by local wall-side oxygen consumption, and is only weakly dependent on blood-side mass transfer effects.

The second and third observations suggest that wall-side oxygen mass transfer resistance is much larger than blood-side resistance. If this is true, oxygen tension at the blood-wall interface should be only weakly dependent on hemodynamic effects. Figure 7(*b*) shows intimal oxygen tension versus axial position for all five cases. Local hemodynamic effects are observable in this figure. For example, in all five cases, intimal oxygen tension reaches a minimum just distal to the throat of the stenosis, where oxygen-depleted blood is convected away from the wall at the separation point. However, except for the inaccurate solution obtained by neglecting hemoglobin (Case 5), the magnitude of this spatial variation in intimal oxygen tension is fairly small, with local peak-to-peak changes in oxygen tension of approximately 5–6 mmHg. This local variation is only 12 to 15 percent of the total oxygen tension difference between the incoming blood and the vasa vasorum, consistent with the suggestion that blood-side oxygen mass transfer resistance is small relative to wall-side resistance.

Figure 8 shows how wall thickness affects intimal oxygen tension as a function of axial position (panel (*a*)), and how wall thickness affects oxygen tension along a radial slice at the stenosis throat (panel (*b*)). It is clear that wall thickness has little influence on blood-side oxygen tension, while markedly altering wall-side oxygen profiles. This confirms the dominant nature of the wall-side mass transfer resistance.

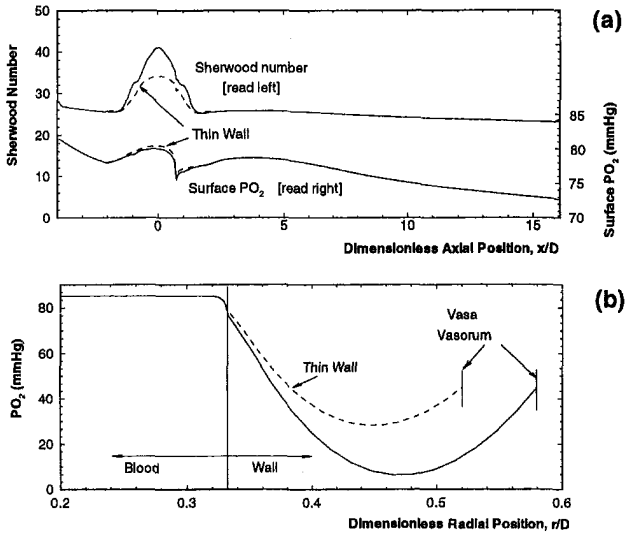

Fig. 8 Comparison of effects of wall thickness on oxygen mass transfer. Panel (*a*): local Sherwood number (upper 2 curves) and surface PO_2 (lower 2 curves) versus axial position in stenosis. Panel (*b*): oxygen partial pressure at the throat of the stenosis versus radial position. Solid lines: thick wall; dashed lines: thin wall. Refer to text for respective wall thicknesses.

4 Discussion

4.1 Blood-Side Modeling of Oxygen Mass Transfer. Our results indicate that linearization of the equation governing blood-side oxygen transport can produce accurate results, subject to the following provisos:

1 Neglecting the oxygen-carrying capacity of hemoglobin, as was done in Case 5, consistently leads to large errors. Inclusion of oxygen transport by oxyhemoglobin is mandatory in blood-side oxygen mass transfer calculations.

2 Oxyhemoglobin transport effects can be treated in a computationally efficient manner by using a linearized approximation to Eq. (3), as was done in Case 2. However, due to the complex shape of the oxyhemoglobin saturation curve, the accuracy of this linearized approach depends on both the working range of oxygen tensions in the blood and the mean oxygen partial pressure, $\overline{PO_2}$, about which the Hill equation is linearized. The present study demonstrates that for boundary conditions that are physiologically realistic for the large arteries (e.g., 60 mmHg wall tension or coupled blood–wall transport), the linearized approach gives excellent results for local oxygen flux (Sherwood number), as judged by the very close agreement with the reference solution (Case 1). For such boundary conditions, we conclude that the linearized formulation is the preferred approach for numerical and analytical modeling of blood-side oxygen transport in the large arteries. In fact, solution of the linearized system is no more difficult than solution of Eq. (1) alone, except that the value of the effective diffusivity will typically be much less than that of D_b. This will tend to produce a higher effective Schmidt number, which is numerically more difficult to handle.

3 The linearized solution generally does a worse job of predicting blood-side concentration fields than it does in predicting local Sherwood number distribution (for example, compare Figs. 4(*a*) and 4(*b*)). Thus, care should be taken when using the linearized form of the governing equation if accurate information about blood-side oxygen tension (rather than simply oxygen flux at the wall) is required. The large discrepancy in blood oxygen tension distribution shown in Fig. 4 is puzzling in light of the more modest disagreement in local Sherwood number profiles for these two cases shown in Fig. 3. This can be understood as follows. Recall that in Case 2, Eq. (3) is linearized by replacing the terms $1 + ([\mathrm{Hb}]/\alpha)(dS/dPO_2)$ and $D_b[1 + ([\mathrm{Hb}]/\alpha)(D_c/D_b)(dS/dPO_2)]$ by constants, obtained by evaluating each term at a reference pressure $\overline{PO_2}$. In reality, these terms vary strongly with oxygen tension, and thus vary with position in the mass transfer boundary layer. This causes the effective diffusivity within the mass transfer boundary layer to change with position, an effect not captured with the linearized form of the equation (Case 2). This leads to local compression and distortion of the isoconcentration contours in the mass transfer boundary layer in the linearized case as compared to the reference solution. However, the *overall* mass transfer boundary layer resistance, since it is based on averaged values over the entire boundary layer, is less sensitive to local effects, and is thus reasonably well captured in the linearized form of the equations.

We also found that reducing the Schmidt number by a factor of 100 to 1000 can give qualitatively reasonable results if the Sherwood number is scaled by $Sc^{1/3}$. However, arbitrarily reducing the Schmidt number causes much of the hemodynamically driven local variations in oxygen wall flux to be lost. It also produces large errors in the blood-side oxygen tension distribution. Further, calculations performed at very low Sc (order one to several hundred) in separated flows can give results which are quantitatively and *qualitatively* different from those at higher Sc. For example, for low Sc the maximum Sherwood number in a recirculation zone distal to a contraction scales as $Sc^{-0.58}$ [20], instead of the $Sc^{1/3}$ dependence seen at higher Sc. Also, the location of this maximum Sherwood number varies quite dramatically with Sc [20, 21], but is essentially fixed at higher Sc. For all of these reasons, use of reduced Schmidt numbers should be avoided if at all possible.

4.2 Blood-Wall Coupling of Oxygen Mass Transfer. The most important conclusions of this study are: (*i*) Wall-side oxygen mass transfer resistance generally dominates blood-side resistance, meaning that hemodynamic effects are of secondary importance; and (*ii*) local wall-side oxygen demand determines local wall flux. The first conclusion contradicts estimates made by Back [7], but agrees with the calculations of Stoop et al. [15]. Because of these facts, use of a constant oxygen tension boundary condition at the blood–wall interface can lead to highly misleading conclusions. For example, results from the 60 mmHg constant wall tension simulations indicated that there is approximately a sevenfold variation in blood-side mass transfer resistance due to local hemodynamic effects (Table 1). However, because the blood-side mass transfer resistance is small compared to wall-side resistance, this large local variation in blood-side resistance translates into only a weak dependence of intimal oxygen tension on hemodynamic effects. In this study, such local variations were on the order 5–6 mmHg. It is unclear as to whether such local variation in oxygen tension, maintained chronically, is physiologically significant.

In order to conceptualize better the physics of oxygen mass transfer in the coupled blood–wall case, we have found it useful to use a simple lumped parameter electrical analogue model of the mass transfer process, as shown in Fig. 9. This incorporates

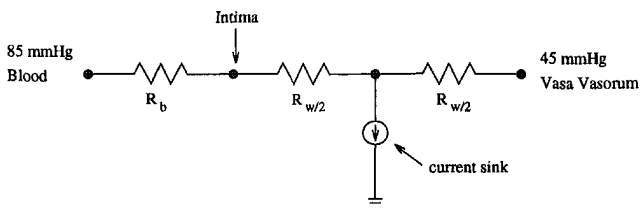

Fig. 9 Simplified lumped parameter model of the physical processes occurring during oxygen mass transfer. R_b is blood side mass transfer resistance; $R_{w/2}$ is mass transfer resistance of half of wall; current sink represents oxygen consumption by wall tissue.

the effects of blood-side and wall-side mass transfer resistance (R_b and R_w, respectively), as well as oxygen consumption by the wall. When $R_w \gg R_b$, intimal PO_2 is only weakly dependent on R_b.

Because oxygen flux and intimal oxygen tension depend critically on local oxygen consumption, modeling of oxygen consumption will be important in any future studies of oxygen transport in large arteries. Local oxygen consumption depends both on local thickness of the avascular region of the wall (intima to vasa vasorum), and on the volumetric consumption rate, $\dot{q}$. Both of these can be expected to change from normal values in diseased regions. In particular, the tissue oxygen consumption rate will be strongly affected by the composition (particularly cellularity) and metabolic demands of pathological regions. In this context, it is particularly interesting to note that the wall thickness (lumen to vasa vasorum) of the model shown in Fig. 1(a) is close to the maximum thickness of oxygen-consuming wall that can be supported. As indicated by the radial PO_2 profiles at the stenosis throat (Fig. 8(b)), a minimum PO_2 value is reached within the thickened wall tissue. When calculations were carried out in models with even thicker walls, this minimum value approached 0 mmHg. Physiologically, this effect would be counterbalanced by proliferation of vasa vasorum within the adventitia and necrosis within the core of the plaque region. This accords with experimental evidence indicating that in severely thickened arteries, sufficient vasa proliferation will occur to maintain a minimum wall PO_2 of 15 mmHg [2].

It is important to mention some of the limitations of this study. We have assumed that the kinetics of oxygen exchange between oxyhemoglobin and free (plasma) oxygen are much faster than any other time scale in the problem. This assumption seems reasonable, since the time scale for oxygen exchange between red cells and plasma will be the diffusion time associated with a red cell characteristic dimension. This is expected to be very rapid.

In this study we have also only addressed steady flow. Physiological blood flow is strongly pulsatile, and significant temporal variation in mass transport would be anticipated for models with constant wall concentration boundary conditions [7]. However, it has been shown that oxygen consuming arterial walls act to dampen the effect of pulsatility [13, 16], and oxygen transport well within the artery wall is likely not strongly influenced by flow field pulsatility. However, pulsatility will influence oxygen transport in the immediate vicinity of the intima [16]. Physically, pulsatility is expected to cause localized zones of extreme (high and low) blood-side mass transfer resistance to move about in the artery, yielding time-averaged blood-side mass transfer resistances that are less spatially variable than in the steady case. This would further reduce the importance of localized blood-side mass transfer effects.

We have also studied flow at relatively low Reynolds number, which is slightly unrealistic for the large arteries in humans. However, increasing the Reynolds number would tend to reduce blood-side mass transfer resistance (especially if turbulence were generated distal to the stenosis), and thus our conclusions about the relative importance of blood-side and wall-side mass transfer resistance would be strengthened. Another hemodynamic simplification is the assumption of Newtonian blood rheology. Hemodynamic studies comparing the effects of non-Newtonian versus Newtonian rheology generally find modest (20 percent or less) differences in wall shear stress (see, e.g., [22]). Inclusion of non-Newtonian blood rheology would therefore be expected to result in small changes in blood-side mass transfer resistance compared to the Newtonian case, but would not affect the main conclusions of the study.

Finally, and most importantly, these conclusions are only relevant for small molecules whose transmural filtration velocities are much smaller than their diffusion velocities. This would not be the case for larger molecules, such as LDL, where transmural convective effects are very significant. Localized hemodynamic effects in the transport of such molecules are potentially very significant [23].

Acknowledgments

This work was supported by NSERC Collaborative Grant No. CPG0163599 (CRE). JAM was supported by an NSERC Graduate Scholarship and the Canadian Federation of University Women.

References

1 D. W. Crawford and D. H. Blankenhorn, "Arterial wall oxygenation, oxyradicals, and atherosclerosis," *Atherosclerosis,* Vol. 39, 1991, pp. 97–108.

2 T. Zemplenyi, D. W. Crawford, and M. A. Cole, "Adaptation to arterial wall hypoxia demonstrated in vivo with oxygen microcathodes," *Atherosclerosis,* Vol. 76, 1989, pp. 173–179.

3 H. A. Massaldi and A. C. Taquini, "Haemodynamics and arterial wall metabolism: their possible combined role in atherogenesis," *Medical Hypothesis,* Vol. 35, 1991, pp. 210–218.

4 D. P. Hajjar, I. C. Farber, and S. C. Smith, "Oxygen tension within the arterial wall: relationship to altered bioenergetic metabolism and lipid accumulation," *Arc. Biochem. and Biophys.,* Vol. 262(1), 1988, 375–380.

5 S. G. E. Barker, A. Talbert, S. Cottam, P. A. Baskerville, and J. F. Martin, "Arterial intimal hyperplasia after occlusion of the adventitial vasa vasorum in the pig," *Arterio. and Thromb.,* Vol. 13, 1993, pp. 70–77.

6 D. G. Buerk and T. K. Goldstick, "Arterial wall oxygen consumption rate varies spatially," *Am. J. Physiol.,* Vol. 243, 1982, pp. H948–H959.

7 L. H. Back, J. R. Radbill, and D. W. Crawford, "Analysis of oxygen transport from pulsatile viscous blood flow to diseased coronary arteries of man," *J. Biomech.,* Vol. 10, 1977, pp. 763–774.

8 G. Schneiderman and T. K. Goldstick, "Significance of luminal plasma layer resistance in arterial wall oxygen supply," *Atherosclerosis,* Vol. 31, 1978, pp. 11–20.

9 G. Schneiderman, C. G. Ellis, and T. K. Goldstick, "Mass transport to walls of stenosed arteries: variation with Reynolds number and blood flow separation," *J. Biomech.,* Vol. 12, 1979, pp. 869–877.

10 M. Rappitsch and K. Perktold, "Computer simulation of convective diffusion processes in large arteries," *J. Biomech.,* Vol. 29, 1996, pp. 207–215.

11 E. A. McClelland and D. N. Ku, "An investigation of transient transport phenomena in separated flow," in: M. S. Hefzy, R. M. Hochmuth, and N. A. Langrana, eds., *Proc. Summer Bioengineering Conference,* ASME BED-Vol. 29, 1995, pp. 17–18.

12 C. G. Caro, T. J. Pedley, R. C. Schroter, and W. A. Seed, *The Mechanics of the Circulation,* Oxford University Press, Oxford, 1978.

13 G. Schneiderman, L. F. Mockros, and T. K. Goldstick, "Effect of pulsatility on oxygen transport to the human arterial wall," *J. Biomech.,* Vol. 15, 1982, pp. 849–858.

14 C. K. Colton and R. F. Drake, "Effect of boundary conditions on oxygen transport to blood flowing in a tube," *Chem. Eng. Symp. Ser, Adv. Bioengng.,* Vol. 67(114), 1971, pp. 88–95.

15 M. L. M. Stoop and P. H. M. Bovendeerd, "The influence of steady fluid flow on solute transfer in a two-dimensional carotid artery bifurcation," in: R. Vanderby, Jr., ed., *1991 Bioengineering Conference:* BED-Vol. 20, 1991, pp. 223–226.

16 L. H. Back, "Analysis of oxygen transport in the avascular region of arteries," *Math Biosci.,* Vol. 31, 1976, pp. 285–306.

17 W. W. Nichols and M. F. O'Rourke, *McDonald's blood flow in arteries,* Lea & Febiger, Philadelphia, 3rd ed., 1990.

18 T. R. Stein, J. C. Martin, and K. H. Keller, "Steady-state oxygen transport through red blood cell suspensions," *J. Applied Physiology,* Vol. 31, 1971, pp. 397–402.

19 D. A. Steinman and C. R. Ethier, "Code testing with an exact solution to the 3D Navier-Stokes equations," in: J. J. Gottlieb and C. R. Ethier, eds., *Proc. CFD 94,* 1994, pp. 115–122.

20 D. F. Fletcher, S. J. Maskill, and M. A. Patrick, "Heat and mass transfer computations for laminar flow in an axisymmetric sudden expansion," *Computers and Fluids,* Vol. 13, 1985, pp. 207–221.

21 P. Ma, X. Li, and D. N. Ku, "Heat and mass transfer in a separated flow region for high Prandtl and Schmidt numbers under pulsatile conditions," *Int. J. Heat and Mass Transfer,* Vol. 37, 1994, pp. 2723–2736.

22 D. A. Steinman, P. D. Ballyk, and C. R. Ethier, "Simulation of non-Newtonian blood flow in an end-to-side anastomosis," *Biorheology,* Vol. 31, 1994, pp. 565–586.

23 X. Deng, M. W. King, and R. Guidon, "Localization of atherosclerosis in arterial junctions: Concentration distribution of low density lipoproteins at the lumenal surface in regions of disturbed flow," *ASAIO Journal,* Vol. 41, 1995, pp. 58–67.

24 R. B. Bird, W. E. Stewart, and E. N. Lightfoot, *Transport Phenomena,* Wiley, New York, 1960.